Gil-Santos, A.; Marco, I.; Moelans, N.; Hort, N.; van der Biest, O.:

Microstructure and degradation performance of biodegradable Mg-Si-Sr implant alloys

In: Materials Science and Engineering C (2016) Elsevier

DOI: 10.1016/j.msec.2016.09.056

Microstructure and degradation performance of biodegradable Mg-Si-Sr implant alloys

Andrea Gil-Santos[1], Iñigo Marco[1], Nele Moelans[1], Norbert Hort[2], Omer Van der Biest[1]

[1]Department of Materials Engineering, KU Leuven, Kasteelpark Arenberg, 44, 3001 Leuven, Belgium
[2]Magnesium Innovation Centre (MagIC), Helmholtz-Zentrum Geesthacht, Max-Planck-Strasse 1, 21502 Geesthacht, Germany

e-mail corresponding author: andrea.gilsantos@mtm.kuleuven.be, andrea.gil.santos@hotmail.com

Abstract

In this work the microstructure and degradation behavior of several as-cast alloy compositions belonging to the Mg rich corner of the Mg-Si-Sr system are presented and related. The intermetallic phases are identified and analyzed describing the microstructure evolution during solidification. It is intended in this work to obtain insight in the behavior of the ternary alloys in *in vitro* tests and to analyze the degradation behavior of the alloys under physiologically relevant conditions. The as-cast specimens have been exposed to immersion tests, both mass loss (ML) and potentiodynamic polarization (PDP). The degradation rate (DR) have been assessed and correlated to microstructure features, impurity levels and alloy composition. The initial reactions resulted to be more severe while the degradation stabilizes with time. A higher DR is related with a high content of the $Mg_{17}Sr_2$ phase and with the presence of coarse particles of the intermetallics Mg_2Si, MgSiSr and $MgSi_2Sr$. Specimens with a higher DR typically have higher levels of impurities and alloy contents.

Keywords: Magnesium alloys; microstructure; physiological degradation; corrosion layer; intermetallics; impurities.

1. Introduction

Mg based alloys are promising candidates for use as biodegradable implant materials. They have been investigated for the last decades [1, 2] and still new systems are under investigation [3-5]. It was intended in this work to explore a novel Mg-Si-Sr alloy system. The repercussion of the implant

on the human body was considered before selecting Si and Sr as alloying elements. For instance Si contributes to the growth and development of bone and connective tissue [6] and Sr addition enhances new bone formation and increases bone quality around the implant [7, 8]. From the biological point of view, it is favorable that the implant material induces new bone formation, showing a good biocompatibility between the implant and the tissue [9, 10]. This biocompatibility has been observed for Sr or Si in previous *in vivo* studies [3, 6, 11, 12].

The degradation behavior of Mg alloys is rather unpredictable due to many influencing parameters and corrosion product formation [13-16]. Under physiological conditions, those corrosion products accumulate on the alloy surface creating a corrosion layer that may cover it [17]. This layer plays a protective role by retarding or avoiding further degradation [18]. On the one hand polarization experiments with a rotating disk electrode (RDE) [19, 20] have been performed to get data of the material-electrolyte system when the corrosion layer (CL) still does not play a role. This corresponds to the early or initial DR. On the other hand, the DR has been determined by mass loss (ML) method [21]. These values represent the long term degradation response of the materials. However, the reliability of the combination of these two methods to interpret their results is still not confirmed. The use of different methods to calculate the DR has generated opposite trends in previous works. In the work of Chou et al. [22] potentiodynamic polarization measurements generate lower values of DR than ML tests for Mg-Y-Ca-Zr alloys, but the opposite happens for a different material (Mg-Ca-Zn-Mn-Si) in the work from Lisitsyn et al. [23]. Hence, this is identified as a field for further investigation.

Ultrahigh purity Mg has been proven to degrade very slowly (10 µm/year) *in vivo* and *in vitro* [24]. The presence of impurities modifies this behavior, accelerating the degradation of Mg and Mg based alloys [24-27]. Hanawalt et al. [27] presented the effects of different impurities on the resulting DR of Mg based materials in NaCl solutions. In their work the effect of impurities is analyzed (Figure 1) and tolerance limits are defined for various impurities, as the concentrations of the impurities above which the corrosion rate of Mg increases dramatically. Their data show that the tolerance of Mg for impurities changes by alloying it with other elements. Different alloy systems may differ in their tolerance limits .

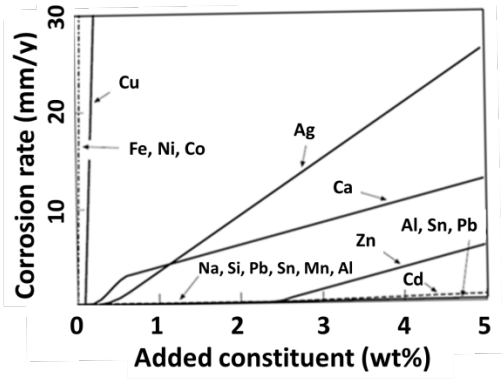

Figure 1. Influence of impurities on the degradation rate of Mg. From reference [28] using the data from [27].

Instead of increasing the Mg purity, alloying Mg is the chosen mechanism to modify the degradation performance [29-32]. The effect of adding Si and Sr is directly related with the compounds that form and their morphology [25]. In particular, Sr acts as a grain refiner when added to Mg alloys due to its tendency to form $Mg_{17}Sr_2$ that accumulates at the grain boundaries [33, 34]. The presence of intermetallics enhances microgalvanic corrosion increasing the degradation rates [35]. As it is indicated by Li et al. [36] the $Mg_{17}Sr_2$ accumulation in grain boundaries increases the DR of Mg-Zr-Sr alloys. However, based on previous results the addition of limited quantities of Sr seems to increase the corrosion resistance . Bornapour et al. [34] indicated amounts smaller than 0.5 wt.% for Mg-Ca-Sr alloys and smaller than 2 wt.% for binary Mg-Sr alloys [11], Brar et al.[35] suggested values between 0.5 and 1 wt.% for Mg-Zn-Sr alloys and Gu et al. [32] defended a 2 wt.% of Sr as the best quantity for binary Mg-Sr alloys.

Si addition into Mg alloys leads to the formation of Mg_2Si precipitates. When Mg_2Si forms in its coarse morphology, it decreases the corrosion resistance [37], but the morphology can be modified into a finer by the addition of a third element. Within this finer morphology the detrimental effect that accelerates the DR is reduced. Ben-Hamu et al. [37] reported that the addition of Zn into Mg-Si alloys refines the Mg_2Si phase, improving their corrosion resistance. Srinivasan et al. [38] showed that under static conditions the presence of fine Mg_2Si reduces the corrosion potential compared with the non-refined compounds in Mg-Si-Zn alloys, it reduces the DR. This refinement effect on the Mg_2Si phase by adding Ca or Sr to Mg-Si alloys has been reported by Zhang et al. [6] and Mingbo and Jia [39]. In our case by the simultaneous addition of Si and Sr the ternary phases MgSiSr and $MgSi_2Sr$ may also appear [40] but there is no information on the influence of these ternary phases on the degradation behavior reported yet.

2. Materials and methods

2.1 Alloy production

All the castings were processed by permanent mold gravity casting. An electrical resistance furnace under a mixed protective atmosphere of Ar and 2 vol.% SF_6 was used to melt the alloys. The raw materials consisted of Mg ingots (99.9 %), Si granulates (<6mm, 99.9 % purity from Chempur) and Sr chips (3-12mm, 99.9 % purity from Alfa Aesar packaged in high purity mineral oil). Initially the solid Mg was molten in a mild steel die by heating it up to 700°C. When molten, the pre-heated Si granulates at 400°C were added and the mixture was stirred with a steel paddle every 5 minutes to improve the homogeneity. The mixture was maintained at 700°C for 20 minutes in order to favor the solubility of Si. Then, preheated Sr chips at 400°C were added to the melt after which an exothermic reaction occurred rising the temperature of the melt up to values between 750 and 850°C. If oxide products were formed on top of the melt they were removed. When the temperature of the melt was cooled down to 700°C the molten alloy was poured into a preheated mild steel die (20 cm long and 1.8 cm diameter) previously held at 400°C. Hexagonal BN was used as a mold release agent. After two minutes, the die was opened and the alloy was cooled down to room temperature in air.

2.2. Microstructure study

Disk shaped specimens for microstructural characterization were cut with 2 mm height and 18 mm diameter from the center of the 20 cm long cast specimens. These disk samples were then ground with silicon carbide emory papers by wet grinding from 800 to 2500 mm grain size and later polished with water-free colloidal silica solution (0.2 µm particle size). The etching agent used was picric acid based, containing 10 mL of acetic acid, 4.2 g of picric acid, 20 mL H_2O and 50 mL ethanol and the etching time was between 5 and 10 seconds. In the cases where grains were not revealed after etching and under polarized light, the use of electron back scattered diffraction (EBSD) was needed in order to differentiate the grains. The average grain size was measured by Image-Pro Plus 6.0 image software (Media Cybernetics Inc., Rockville, USA) from optical microscope images of the etched surfaces. The linear intercept method according to ASTM: E112-13 (2013) was used.

The microstructure and the intermetallic compound presence was analyzed using an optical microscope and a Philips XL30 FEI scanning electron microscope (SEM) equipped with an EDAX TSL energy dispersive X-ray spectroscopy (EDS) detector. Backscatter electron (BSE) mode was used for the phase identification. The small size of the particles made it difficult to determine the compounds stoichiometry and an XRD analysis was then carried out in a XRD Seifert 3003-TT in order to verify the existence of the identified phases. Cu-Kα radiation was used at 40kV and 40 mA, from 20 to 80 degrees with a 0.02 step size and a measurement time of 2 seconds per step. The phase

identification was done by comparison with the JCPDS cards included in the Pearson database. The used cards for Mg, Mg_2Si, $Mg_{17}Sr_2$, MgSiSr and $MgSi_2Sr$ are identified with the numbers 00-035-0821, 00-035-0773, 03-065-3649, 01-089-1920 and 01-087-0897. Due to the low amount of compounds compared to the Mg matrix some of the peaks are covered by the Mg ones which are always the dominating peaks. Nevertheless, characteristic peaks for the different intermetallic phases could be identified in the XRD patterns.

Image analysis was carried out on SEM micrographs to measure the volume fraction of each phase using ImageJ software (version 1.47v, Wayne Rasband). The different phases were identified based on their diverse shapes and atomic number contrast provided by the back scatter detection mode. Several micrographs were used for every sample to estimate the average volume fraction of each phase.

The analysis of the solidification process and microstructures is supported with thermodynamic calculations, using the Scheil model for non-equilibrium solidification. More specifically, the Scheil model assumes that the diffusion in the liquid is infinitely fast [41, 42] while that in the solid is negligible [43]. These simulations are performed using Pandat 2016.1 software with the internally developed MgSiSr_v7_rsf database [44].

2.3. Degradation tests

Polarization experiments with Rotating disc electrode (RDE) have been performed with the sample surfaces in contact with phosphate buffered saline (PBS, Sigma Aldrich) solution. The mass loss (ML) immersion tests were done in Dulbecco's Modified Eagle's Medium (DMEM, Merck) with the addition of 10 vol.% of fetal bovine serum (FBS). Both, PBS and DMEM solutions, are commonly used in research for bioabsorbable Mg implant degradation studies [45, 46]. These media can simulate the human body fluid composition and pH, as they represent a similar environment that the implants will face in a real application. The compositions of the different media are summarized in Table II.

Table II. Ionic composition of PBS, FBS and DMEM used for biodegradation testing in mmol/L.

	Na^+	K+	Cl-	HCO_3^-	$H_2PO_4^-$	HPO_4^{2-}	Fe^{2+}	Mg^{2+}	Ca^{2+}
PBS	154.1	4.1	140.6	--	1.5	8.1	--	--	--
DMEM	155.3	5.3	119.3	44.1	154.0	--	2.5E-04	0.8	1.8
FBS*	138.0	10.5	--	--	2.8	--	29.6	1.4	--

*FBS is mainly proteins, the electrolyte content is the one compared in this table.

Both tests were performed on the same samples, first RDE was applied and after surface preparation, the ML tests were done. Three samples have been analyzed per alloy composition. Average values are presented and considered for the discussions. A schematic picture of both methods is presented in Figure 2 and they are described by Marco and Van der Biest [19] and Tie et al. [3] respectively.

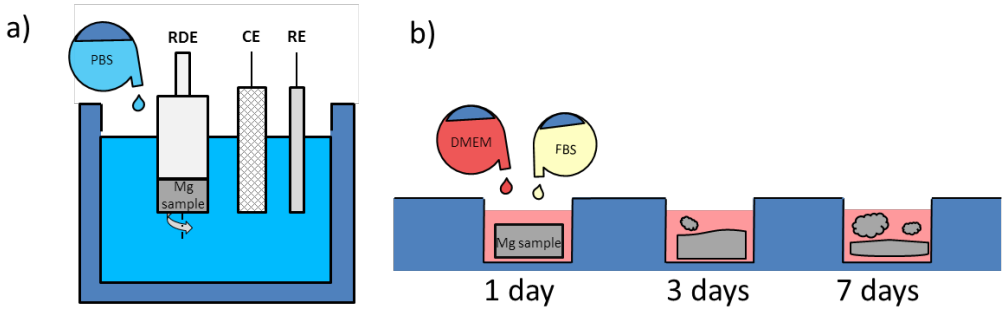

Figure 2. Schematic description of the experimental set-ups for a) Eletrochemical cell used to apply the polarization methods with the rotating disc electrode (RDE) as working electrode (WE), platinum mesh as counter electrode (CE) and Ag/AgCl as reference electrode (RE) from [19]. and b) immersion tests on DMEM with 10vol.% FBS media where samples were weight after and before testing [3].

2.3.1. Polarization experiments

RDE procedure (Figure 2a) is based on potentiodynamic polarization (PDP) tests. With a RDE the working electrode holding the sample is in motion generating a fluid flow that avoids the deposition of corrosion products. A standard three-electrode cell was employed for all measurements in phosphate buffered saline solution (PBS). Pt was used as the counter electrode, Ag/AgCl as the reference electrode and the sample was the working electrode prepared in a rotating disc. The working electrode had an exposed surface of 50 mm^2 and it rotated at 2000 rpm, providing a stable flow for more reproducible data. The temperature of the solution was maintained at 37 ± 0.5°C and the pH was stable within the range of 7.4 to 7.8. The samples were immersed while they were already in rotation, to minimize the possibility of a corrosion layer (CL) formation. The open circuit potential (OCP) measurement started immediately after immersion, to check the stability of the potential and to make sure that air bubbles do not perturb the measurements. The PDP was then started and the consecutive PDP had a time interval of 5 s approximately. The scanned potential range of ± 500 mV around the OCP (which was about 1.7 and 1.8 V) was done with a scan rate of 1 mV/s. The test finished once the range was measured and then samples were removed, rinsed in ethanol and dried.

In order to calculate the corrosion current density, the Tafel extrapolation was applied [47]. To determine both the anodic and cathodic slopes, the Tafel fit was applied for the measured voltages

of ±500 mV around the corrosion potential. This analysis was carried out using the CorrView-3.3c software (by Scribner Associates, Inc., USA). From the two slopes intersection the corrosion current (i_{corr}) was estimated and the DR was calculated from Faraday's law as shown in equation 1.

$$DR\ \left(\frac{mm}{year}\right) = M_{mol}\left(\frac{g}{mol}\right)\frac{i_{corr}*3600*24*365*10}{n_e*F\left(\frac{C}{mol}\right)\rho\left(\frac{g}{cm^3}\right)} = 3{,}1536\ \cdot 10^8\ \frac{i_{corr}\,M}{n\,F\,\rho} \quad [1]$$

Where i_{corr} is the current density in A/cm^2, M_{mol} is the molecular mass for the Mg alloy which will be considered as 24.31$\frac{g}{mol}$, n_e the number of electrons exchanged between the electrochemical reactions which is 2 (Mg^{2+} ions), *F* is the Faraday's constant (96,485 C/mol) and Mg density is $\rho = 1.74\left(\frac{g}{cm^3}\right)$

2.3.2. Mass loss tests

DR by ML procedure (Figure 2b) is based on the ASTM G31-72 [21] and described as follows. First the sample surfaces were ground with up to 2500mm SiC emery paper for a time sufficient to remove traces from the RDE preceding experiments. Then the samples are weight so that the initial weight can be used as the reference. They are cleaned during 20 minutes by ultrasounds in an ethanol (100%) sonication bath. After drying they are individually packaged in Ar filled bags which are opened only before testing. The conditions in the incubator are 5 vol.% CO_2, 19.7 vol.% O_2 and 95%rh at 37°C. The immersion medium consists of DMEM with 10 vol.% of FBS. A sufficient amount of immersion medium is added for complete sample immersion (5ml). The immersion medium is replaced every 2 days. The pH of the solution is measured during testing in order to assure similar to *in vivo* conditions. The samples have been exposed to average pH-values of 8.5±0.2. The contact surface of the samples with the immersion medium varied between 310 and 440 mm^2.

After 7 days, the samples are washed with deionized water and the formed corrosion products are removed using a chromic acid treatment (180 g of chromium oxide in 1L of distilled water). As for the sample size used in this study, some of the specimens got completely transformed into corrosion products within 7 days of immersion time, this testing period was considered to be the most appropriate for a DR comparison between the different sample compositions. The samples are immersed in the chromic acid solution during 20 minutes. When corrosion products are still remaining on the surface after this time, the immersion time is increased. After this procedure samples are weighted. The DR is calculated using equation 2 where DR is the degradation rate in mm/year, the constant $k = 8.76\ 10^4$, ΔW is the difference between the weights measured before and after the immersion test in grams, A is the sample area exposed to solution in cm^2, t is the time of exposure in hours and ρ is the density of the material in g/cm^3.

$$DR = k\frac{\Delta W}{At\rho} \quad [2]$$

3. Results and discussion

The discussed results come from nine alloy compositions. The specimens have been tested and compared in as-cast condition. Their compositions and impurity contents are presented in Table I.

Table I. Compositions and trace elements of the alloys in wt.%. Analysis done by inductively coupled plasma optical emission spectroscopy (ICP-OES, Varian 720 ES) in one representative sample for each alloy composition.

Alloy name	Composition (wt. %)		Impurities (wt%)						
	Si	Sr	Al	Ca	Cu	Fe	Mn	Ni	Total
A. Mg 1.26Si 12.29Sr	1.26	12.29	0.006	0.021	6E-4	0.010	0.012	<1E-4	0.05
B. Mg 0.67Si 10.30Sr	0.67	10.30	0.006	0.023	6E-4	0.010	0.011	<1E-4	0.05
C. Mg 1.53Si 8.92Sr	1.53	8.92	0.005	0.018	6E-4	0.009	0.012	1E-4	0.04
D. Mg 5.17Si 2.87Sr	5.17	2.87	0.005	0.013	8E-4	0.006	0.025	2E-4	0.05
E. Mg 3.83Si 2.64Sr	3.83	2.64	0.002	0.005	7E-4	0.012	0.002	2E-4	0.02
F. Mg 0.55Si 0.75Sr	0.55	0.75	0.004	0.004	3E-4	0.005	9E-4	6E-4	0.02
G. Mg 0.29Si 0.75Sr	0.29	0.75	0.002	0.004	6E-4	0.005	0.002	7E-4	0.01
H. Mg 0.13Si 0.25Sr	0.13	0.25	0.001	0.003	7E-4	0.003	0.002	7E-4	0.01
I. Mg 0.14Si 0.07Sr	0.14	0.07	0.001	0.001	5E-4	0.007	0.001	2E-4	0.01
Pure Mg	0.006	4E-4	0.002	0.032	5E-4	0.035	0.005	5E-4	0.04

3.1. Microstructure study

The binary compounds Mg_2Si and $Mg_{17}Sr_2$ and ternary compounds MgSiSr and $MgSi_2Sr$ were found in the different microstructures. The combination of phases present in the specimens for the different alloy compositions deviates in many cases from the expected equilibrium phases, indicating that the alloys followed a non-equilibrium solidification path during casting. For the further discussion, three different alloy groups are distinguished based on the phases present in the as-cast microstructures. The first alloy group consists of the alloys in which the intermetallic phases $Mg_{17}Sr_2$, MgSrSi and $MgSi_2Sr$ are present. The second group contains the alloys in which the Mg_2Si and $MgSi_2Sr$ phases are present and for the third group of alloys the compounds $Mg_{17}Sr_2$ and MgSiSr are present. In order to

make the analysis easier the intermetallic names are shortened to a few characters, as it was done in a previous work on this system [40], and they will be referred as listed in Table III.

Table III. Intermetallic compound names and their identification, as taken from reference [40].

Intermetallic compound	Name
$Mg_{17}Sr_2$	M17
Mg_2Si	M2
MgSiSr	M111
$MgSi_2Sr$	M121

The specimens are separated according to the defined alloy groups. The alloys A, B and C belong to the first group. The alloys D, E and F are included in the second group and alloys G and H are in the third. Finally, for alloy I only the M121 phase appears distributed in the Mg matrix. This classification is indicated in the last column of Table IV.

The phase identification is presented in Figure 3, alloys in the group I in a) the ones in the group II in b) and the ones in the group III in c). By the combination of the two applied techniques (XRD and SEM-EDS) the phase identification was confirmed. The phase identification and quantification for each alloy composition is presented in Table IV.

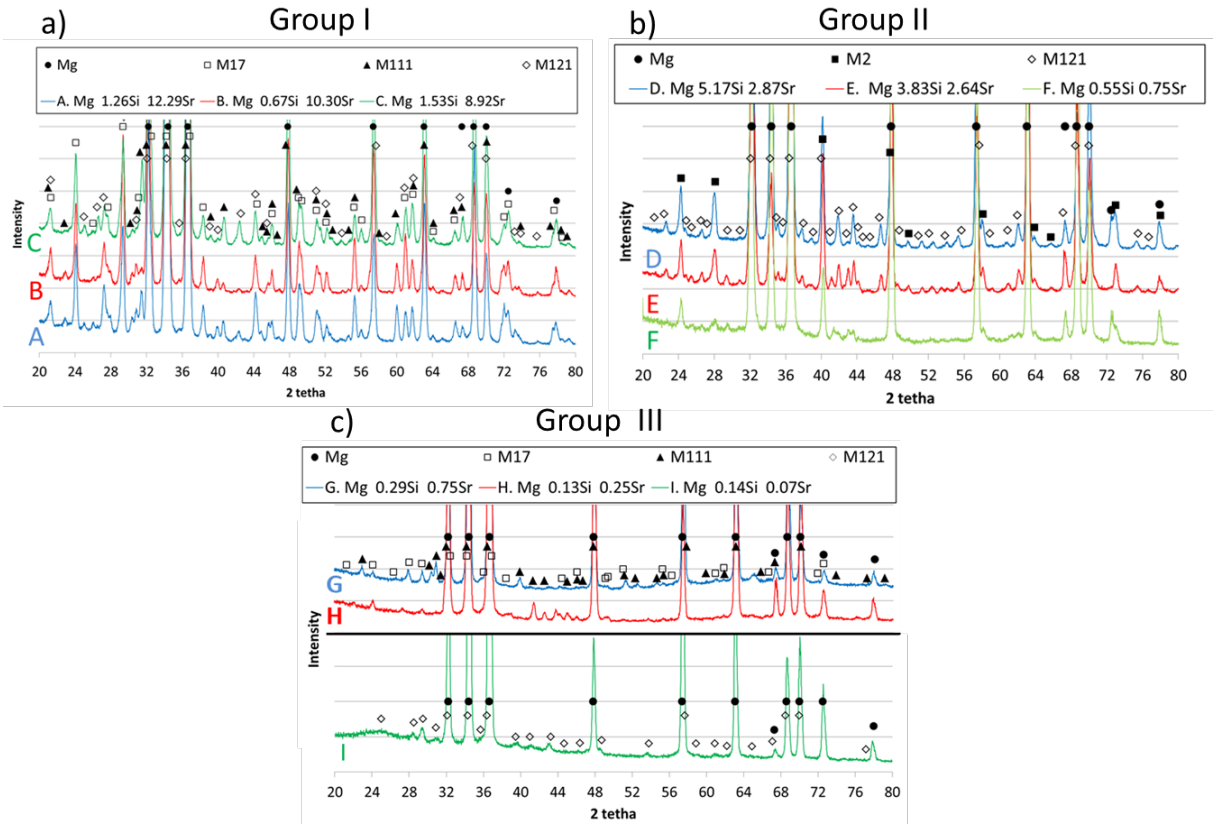

Figure 3. XRD peaks identification for alloys A to I separated by groups.

Table IV. Phase identification for alloys A to I by groups including their phase content in wt.% experimentally measured. Mg content is considered as balance.

Alloy name (wt.%)	Intermetallic phases (wt.%)					Group	Present phases
	M2	M121	M111	M17	Total		
A. Mg 1.26Si 12.29Sr		6.9 ± 0.5	1.6 ± 0.3	31.1 ± 1.9	39.7	I	Mg + M17+ M111 + M121
B. Mg 0.67Si 10.30Sr		1.6 ± 0.4	0.6 ± 0.2	36.6 ± 2.3	38.8		
C. Mg 1.53Si 8.92Sr		6.9 ± 0.4	0.2 ± 0.6	20.5 ± 2.2	27.6		
D. Mg 5.17Si 2.87Sr	4.4 ± 0.7	11.8 ± 1.8			16.1	II	Mg + M2+ M121
E. Mg 3.83Si 2.64Sr	4.2 ± 0.5	10.3 ± 1.3			14.5		
F. Mg 0.55Si 0.75Sr	3.8 ± 0.6	3.8 ± 0.3			7.6		
G. Mg 0.29Si 0.75Sr			2.0 ± 0.3	5.3 ± 1.2	7.2	III	Mg + M17 + M111
H. Mg 0.13Si 0.25Sr			3.5 ± 0.4	1.4 ± 0.4	4.8		
I. Mg 0.14Si 0.07Sr		5.0 ± 0.1			5.0		Mg + M121

The phases have been labeled on the BSD micrographs from SEM (presented in Figures 6, 7 and 9) in order to show their morphology and distribution. It is concluded from them that depending on the alloy composition different morphologies can be expected. These microstructures and phase morphologies can be related to the solidification path. The liquidus projection of the ternary system presented in Figure 4 shows the primary solidifying phase as a function of composition.

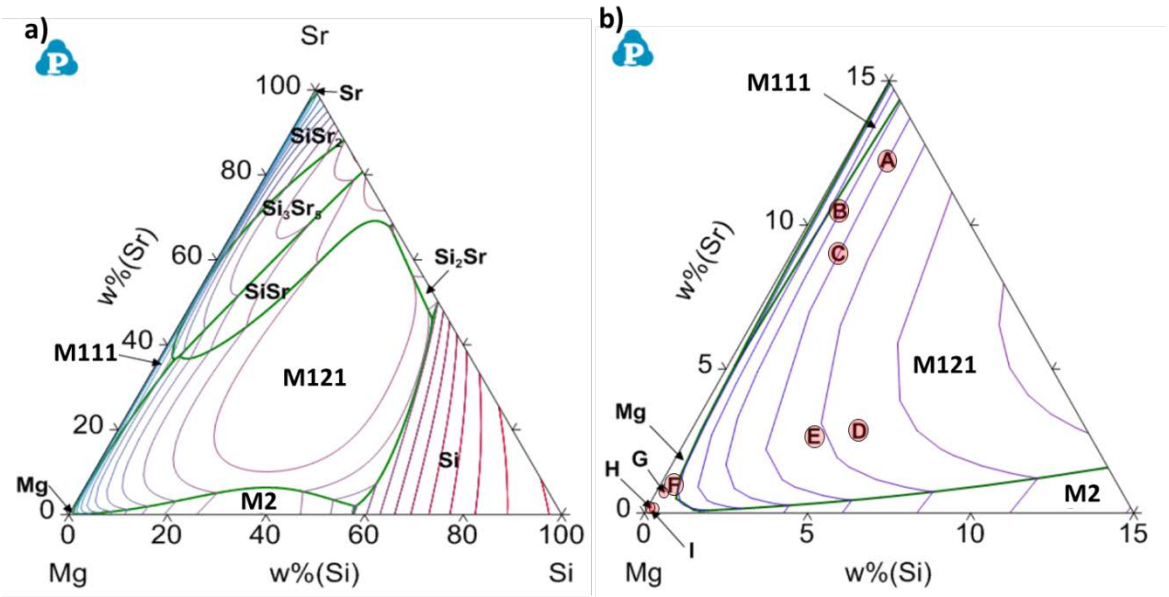

Figure 4. a) Liquidus projection of the Mg-Si-Sr system [44] and b) a zoom on the Mg rich corner showing the location of the studied alloys.

Group I:

In order to relate the size, morphology and distribution of the different phases with the sequence of solidification for these alloys (A to C), a zoom of the microstructure obtained for alloy C is presented in Figure 5. In this Figure, also the phase fractions as a function of temperature obtained from a Scheil solidification calculation for this alloy composition is presented. A cluster of M111 and M121 is captured in the micrograph in Figure 5. The big size M111 and M121 particles and their sharp edges suggest that they solidified first before the solidification of the Mg matrix grains. A primary M121 in light grey is surrounded by the brighter M111, indicating that M111 solidified after M121, as predicted by the Scheil calculations. Once the Si from the liquid was consumed by the formation of ternaries and due to the high amount of Sr in these alloys (from 8.92wt.% to 12.29wt.% in Table III), the remaining liquid will be rich in Sr. This Sr rich liquid accumulates in grain boundaries pushed by the solidifying Mg and will finally solidify simultaneously with M17 in a binary eutectic reaction (the reaction at around 590 °C in figure 5).

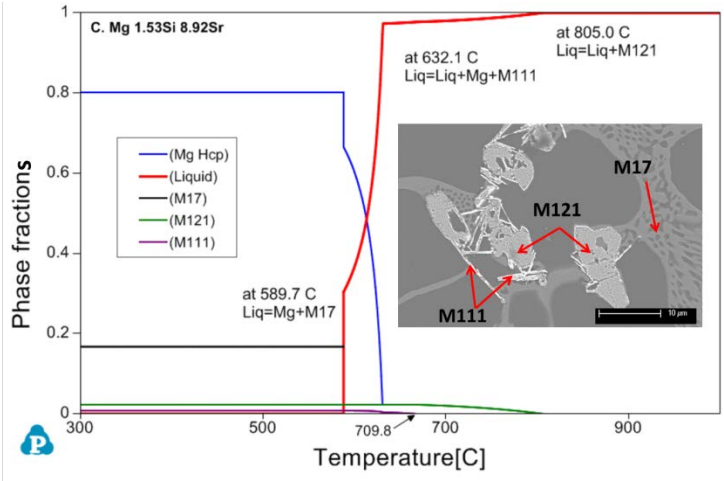

Figure 5. Phase fractions as a function of temperature as calculated from a Scheil solidification model for the alloy composition C. The included micrograph is a higher magnification of alloy C showing a M111 and M121 cluster, indicating that M121 is the primary solidifying phase, followed by the M111 and finalized by the simultaneous appearance of Mg and M17.

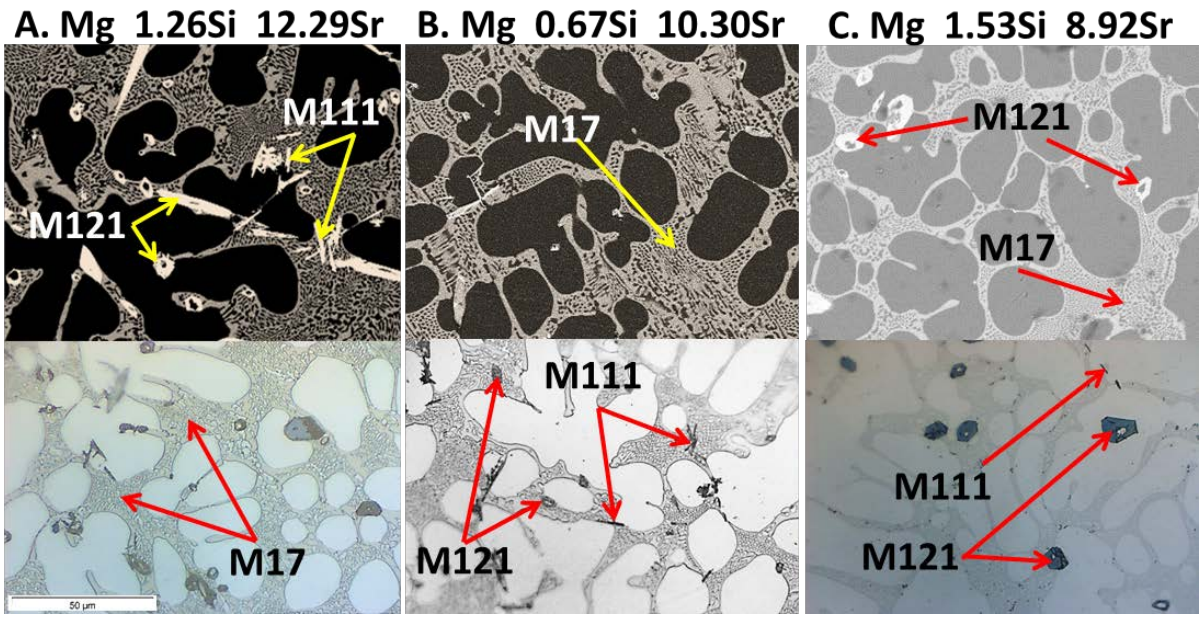

Figure 6. Microstructures from alloys A, B and C from SEM (upper pictures) and from optical microscope after etching (lower micrographs). They show the presence of the M111, M121 and M17 compounds characteristics from the first group.

The microstructures for alloys A to C are presented in Figure 6. The M17 phase has a grey color. It is present in between the Mg matrix islands. The dominant presence of the M17 phase is clear. This phase represents about one third of the total weight per cent of the phase content (Table IV). The large presence of M17 is related with the high Sr content in the alloys; the amount of M17 is the lowest in alloy C (compare to that in alloys A and B) due to its smaller Sr content (Table IV). Furthermore, the amount of the M121 phase that forms in the microstructures seems to be directly related with the amount of Si in the alloy. Alloys A and C, with a higher Si content, namely show a higher amount of this phase (Table IV). M111 in its needle-like shape has a bright white color in the SEM micrographs and its amount decreases from alloy A to alloy C. The possible reason for this trend is that the M111 was formed with the remaining Si after solidification of M121.

Group II:

Representative microstructures obtained for alloys D to F are presented in Figure 7. They show the presence of the M2 and M121 phases, characteristic for the second group of alloys. The M2 particles appear in light grey in the SEM micrographs (Figure 7, upper pictures) and have blue color in the etched micrographs (Figure 7, lower pictures). We distinguish between coarse M2 particles, which are larger than 3 µm, and fine, when smaller. In the same Figure 7, the M121 appears in grey in the etched micrographs and in white in the SEM ones. The M121 particles have been named coarse when bigger than 2 µm and fine otherwise. Alloys D and E contain M2 in two different morphologies,

namely as coarse and fine particles. They also contain coarse M121 precipitates. Alloy F contains the M121 phase in its two morphologies, coarse and finely distributed particles and also shows the M2 phase in its fine morphology. The presence of coarse M2 and M121 is a direct consequence of the higher amount of Si in these alloys. The alloys D and E with 5.17 and 3.83 wt.% Si content show coarse particles while in alloy F with only 0.55 wt.% of Si, the particles are fine.

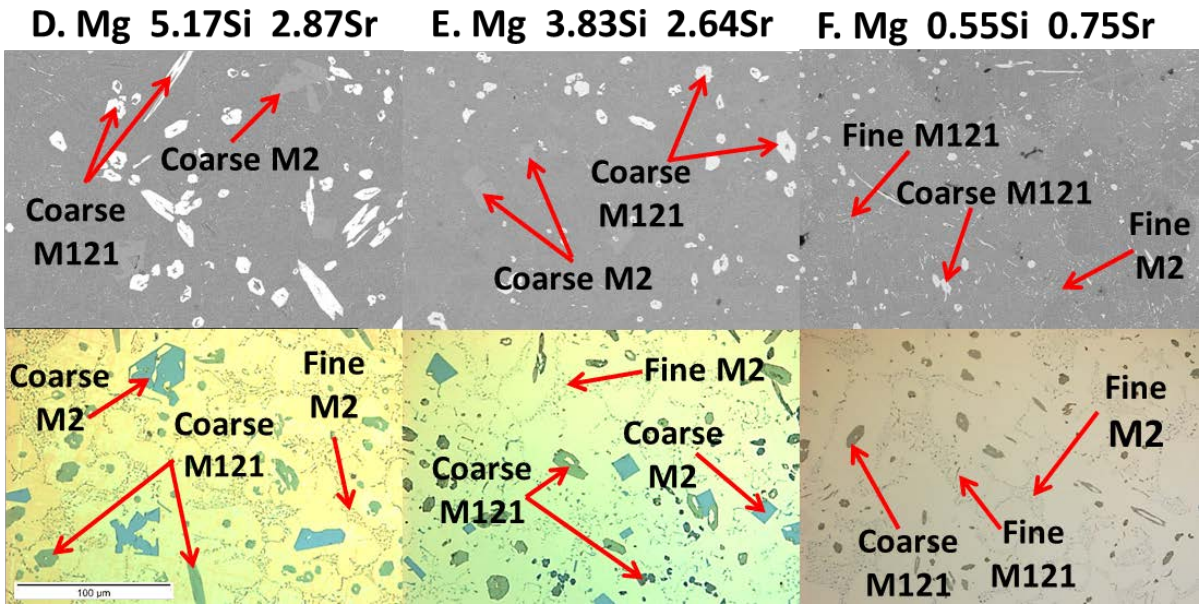

Figure 7. Microstructures from alloys D, E and F from SEM (upper pictures) and optical microscope after etching (lower micrographs). They show the presence of the M2 and the M121. These phases characterize the second group alloys.

The size and shape of the coarse M121 and M2 intermetallics in alloys D and E indicate that they formed from the molten material. From the micrographs (Figure 7) it is difficult to distinguish whether the coarse M2 or the M121 solidified first, but the Scheil solidification calculation for alloy D (Figure 8a) shows that, most likely, M121 is the primary phase forming around 873 °C. Later, the M2 also forms individually from the liquid starting around 727 °C (at this point the amount of M121 is no longer increasing). With the precipitation of M2 and M121, the Sr and most of the Si will be consumed before the start of the Mg solidification. Around 638 °C, Mg and M2 solidify simultaneously in a binary eutectic reaction, producing the M2 formation in its fine morphology distributed in the Mg matrix.

In case of alloy F, the first solidifying phase is Mg; however, practically, almost from the start, Mg solidifies together with M121, according to the Scheil calculation shown in Figure 8b. At a lower temperature (around 637 °C), the remaining liquid undergoes a ternary eutectic reaction forming M121, M2 and Mg. The M121 is observed in brighter color in the SEM micrographs from Figure 7. It

again appears both in a coarse and fine morphology. Most probably, the coarse morphology forms first from the melt, while the fine M121 was formed in the final ternary eutectic reaction together with the fine M2 particles.

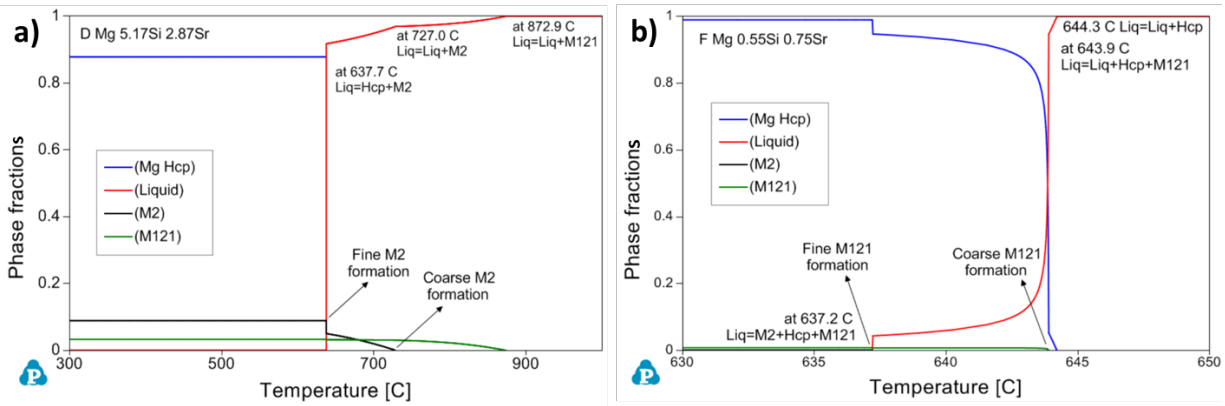

Figure 8. Scheil solidification calculations for the alloy composition D in a) and F in b).

Group III:

Representative microstructures for alloys G, H and I are presented in Figure 9. The micrographs from SEM allow distinguishing visually the presence of the intermetallic phases for these compositions. The M17 phase appears in grey in alloys G and H and it has a globular morphology. The presence of this phase is more evident in alloy G where it is also more interconnected than in H. This effect is correlated with the higher amount of Sr in this alloy. Fine M111 precipitates ($\leq$ 10µm length) are observed in alloys G and H. Their size is bigger in alloy G, which can be related to the higher amount of Si in this alloy. According to the liquidus projection (Figure 4) and the Scheil simulation (Figure 10a) the primary phase for all the alloys in group III is Mg. After Mg, the appearance of the ternaries M121 and M111 is predicted by the Scheil calculations, but only the M111 is observed in the experimental microstructures. The predicted amount of M121 by the Scheil simulations was however very low. The discrepancy between the Scheil model and the experiments could be related to inaccuracies in the database, the model assumptions in the Scheil solidification, or it is possible that the amount of M121 was too small to be detected in the micrographs. Finally, the last liquid solidifies in a binary eutectic reaction forming M17 together with Mg (around 589 °C).

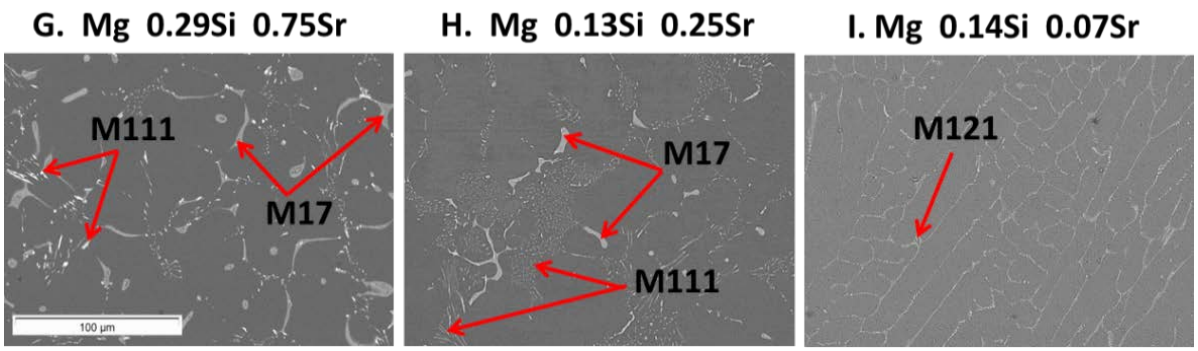

Figure 9. SEM micrographs from alloys G, E and I. G and H show the M17 and M111 compounds characteristic for the group III. In alloy I fine M121 particles are identified in the Mg matrix.

Alloy I consists of the Mg matrix with finely distributed M121 particles (≤ 2µm as defined in group II alloys). According to the liquidus projection (Figure 4) and the Scheil simulation (Figure 10b) Mg is the primary solidifying phase in this alloy. Next, Mg and M121 solidify simultaneously in an invariant reaction (starting around 643 °C). The Scheil calculation further predicts an eutectic reaction at around 638 °C, where also the M2 phase is formed. This phase is however not detected in the final microstructure. A low amount is however predicted (0.24 wt.%) and it may be an inaccuracy of the calculation, but it is also a possibility that it could not have been detected by the employed techniques.

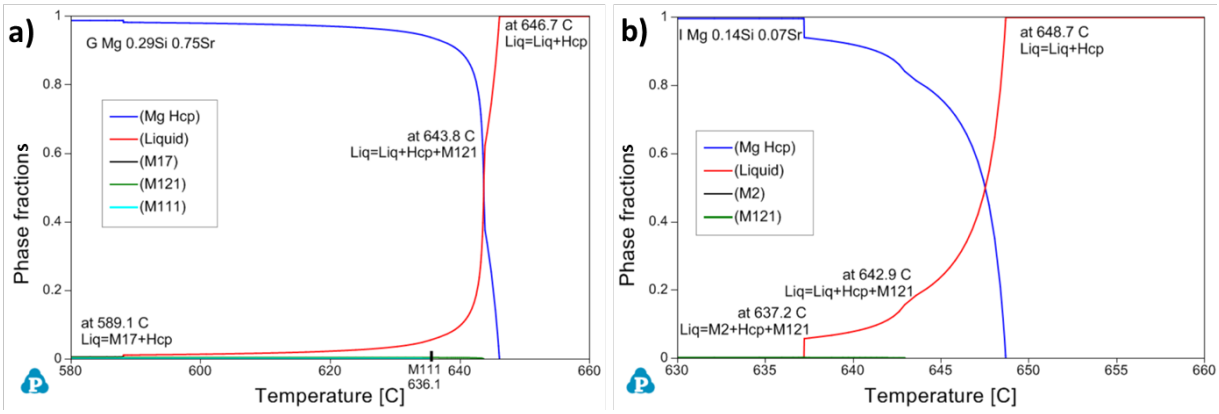

Figure 10. Scheil solidification calculations for the alloy composition G in a) and I in b).

3.2. Degradation performance

3.2.1. Effect of alloying additions

From Figure 11a and Table V a trend can be observed on the dependence of DR on the amount of alloying elements. An increase of the Si and Sr content in general results in a higher degradation rate. For most of the alloys, the DR was larger than that of pure Mg. Some authors (Bornapour et al. [34],

Brar et al. [35] and Gu et al. [32]) have related the presence of a limited amount of Sr to a reduction of the DR compared to that of pure Mg. These previous works refer respectively to the Mg-Ca-Sr, Mg-Zn-Sr and the Mg-Sr systems. The same trend is observed in this work for the Mg-Si-Sr system. The alloys H and I, containing 0.25 and 0.07 wt.% Sr respectively, show a DR smaller than or similar to that of pure Mg (see table V).

Table V. ML and RDE values of DR in mm/year compared to the total amount of alloying elements.

Alloy composition*	Alloy content (wt.%)	DR (mm/year)	
		ML	RDE
E. Mg 3.83Si 2.64Sr	6.47	11.59 ± 4.44	22.09 ± 1.56
F. Mg 0.55Si 0.75Sr	1.30	1.26 ± 0.37	18.25 ± 0.60
G. Mg 0.29Si 0.75Sr	1.04	1.11 ± 0.37	12.65 ± 1.39
H. Mg 0.13Si 0.25Sr	0.38	0.74 ± 0.15	11.85 ± 0.52
I. Mg 0.14Si 0.07Sr	0.21	0.40 ± 0.05	9.33 ± 1.44
Pure Mg	-	0.66 ± 0.36	9.55 ± 1.19

*Alloys A, B, C and D with an alloying element content bigger than 8 wt.% are not included since they degraded faster than 30 mm/year in ML (the entire samples were transformed into corrosion products after 7 immersion days test) making their DR estimation non-reliable.

As the DR clearly increases for Sr contents higher than 0.25 wt.%, a Sr content below 0.25 wt.% is recommended to reduce the DR in this ternary system. The amount of Si also influences the DR and a Si content below 0.15 wt.% is recommended in order to obtain a DR value smaller than that of pure Mg. The total amount of alloying elements (Si + Sr) may be analyzed since both elements are always present in the alloys. Some authors like Cipriano et al. [48] and Bornapour et al. [34] proved that an increase in the DR can be caused by a large addition of a third element such as Sr. From the work of Cipriano et al. when the amount of Sr that is added to Mg-Zn alloys is higher than the solubility of Sr in Mg (between 0.11 and 0.15 wt.%) the DR increases but it only reaches the one of pure Mg at 1.5wt.% Sr and 4wt.% Zn. Then total additions of Zn and Sr below 4.15 wt.% generate DR based on ML slower than that of pure Mg. From the work of Bornapour et al. when the amount of Sr added to Mg-Ca alloys is 0.5 wt.% the DR reaches the value obtained for pure Mg at 0.6 wt.% Ca while an Sr amount of 0.3 wt.% generates a lower DR than that of pure Mg at 0.3 wt.% Ca. Then a total addition of Ca and Sr below 0.9 wt.% will maintain the DR below the one of pure Mg. A similar behavior explains the results obtained in this study. Figure 11a shows that only the specimens with total alloying additions under 0.4wt.% degraded slower or at a similar rate as pure Mg.

It is also observed from Figure 11a (based on data from table V) that the initial DR values are always higher than the ones obtained after long term ML tests. The DR obtained by RDE are about ten times bigger than the ones obtained by ML. This behavior has been observed before by Guan et al. [49] who compared pure Mg and a Mg-Sr-Zn alloy DR by ML tests (Figure 11b). The initially fast DR decreases with time due to the formation of a corrosion layer (CL) on the surface.

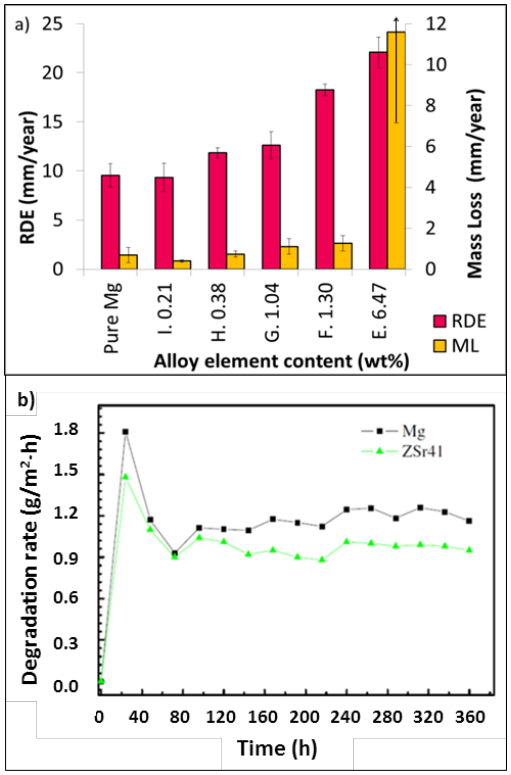

Figure 11. a) Comparison of DR calculated with both RDE and ML techniques in mm/year vs amount of Si and Sr alloying elements in wt.% b) Degradation rates of pure Mg and Mg 4wt.%Zn 1wt.%Sr in simulated body fluid measured by ML at the indicated time intervals from Guan et al. [49].

3.2.2. Effect of impurities

As it is shown in Figure 12a, the DR increases dramatically for impurity levels above 185 ppm. The specimens (about 1 gram of mass and 0.6 cm^3 volume) containing more than the mentioned percentages (samples A to D) got completely transformed into corrosion products within the 7 days of immersion time. Due to the excessive formation of corrosion products, the DR estimation is not reliable for these samples.

From Figure 12, it is clear that there is a tolerance limit in the impurity level, above which the DR increases dramatically. When the DR is measured by ML (Figure 12a), the DR evolution shows the same trend as the curve presented by Song et al. [25]. This behavior, plotted schematically in Figure

12b, shows the influence of the impurity levels of Fe, Ni or Cu on the DR of Mg. The effect of these elements along with Ca is studied in our work, since Hanawalt et al. [27] showed these elements to be impurities which reduces the corrosion resistance (Fig. 1). For these elements, it is also possible to compare Figure 12a with the plot of Song et al. (Figure 12b) to clearly see the tolerance limit effect.

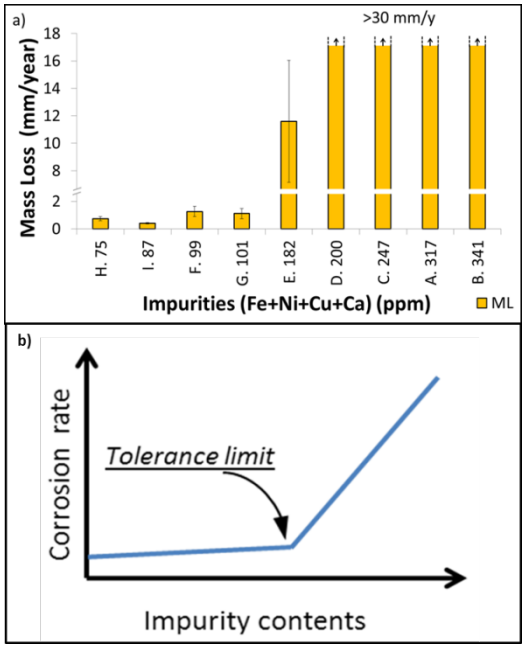

Figure 12. a) Comparison of DR calculated with ML technique in mm/year vs amount of impurities (Fe, Ni, Cu and Ca) in ppm (1wt.%=10000 ppm) and b) Generalized curve showing the influence of element X on the DR (by ML) of Mg, with X=Fe, Ni, Cu. From reference [25].

3.2.3. Relation with the microstructure

As it can be observed in Figure 13a, both initial and long term DR increase with the total amount of intermetallic phases. This effect has been previously related with both impurity level and amount of added Si and Sr but it is going to be analyzed separately considering the influence of intermetallic phases as well.

When the total amount of intermetallic phases is above 14 wt.% the long term DR is higher than 30 mm/year indicating that this large amount of phases is associated with a fast degradation process. In particular, this effect is clearly observed for alloys A to C belonging to the first group of alloys. The main factor that increased the DR value is the high amount of M17 phase in these alloys (>20 wt.% from Table IV). The detrimental effect of the M17 phase in the corrosion resistance was also seen by Brar et al. and Li et al. [35, 36] for Mg-Zn-Sr ternary alloys.

Based on the results from group I alloys (Figure 13a), M17 can cause a high long term DR compared to the initial DR. It has been explained by Bornapour et al. [34] that the presence of intermetallic

phases competes with the presence of a CL. This layer is easily interrupted or cracked at places where intermetallics are located. They explain that significant microgalvanic effects can then generate a non-adherent surface which easily detaches from the CL and the barrier against degradation is lost. In those places where the CL is disrupted the fresh metal surface is exposed and it corrodes again. This mechanism can explain why degradation increases with time when there is a massive presence of the M17 phase.

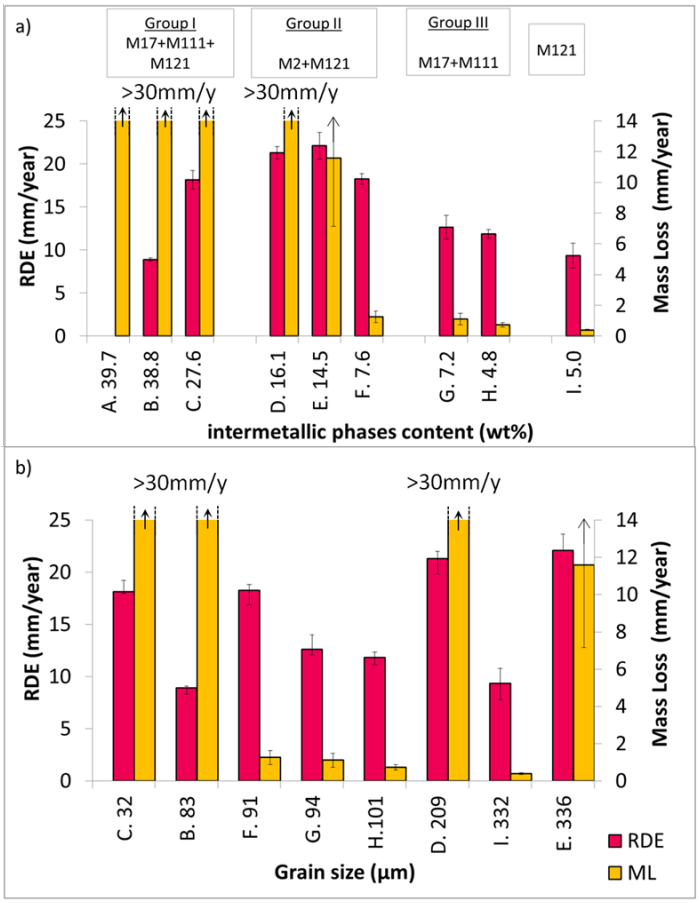

Figure 13. Comparison of DR calculated with both RDE and ML techniques in mm/year as a function of a) wt.% of intermetallic phases considering the different alloy classes and b) increasing grain size.

The highest values of initial degradation were observed for alloys D to F which belong to the second group of alloys. In these cases the presence of coarse polygonal M2 and M121 particles (in blue and in dark grey respectively in Figure 7) possibly facilitate the initial degradation in the interfaces between the Mg matrix and the intermetallic particle edges. Furthermore, a clear difference in DR was observed between sample F and samples D and E. A lower DR was obtained for alloy composition F where the amount of coarse M121 particles is reduced compare to alloys D and E but it may also be related to the morphology of the M2 phase. Big square particles of the binary phase were namely present in alloys D and E while only the fine M2 appeared in alloy F. Based on the work

of Ben-Hamu et al. [37] for Mg-Zn-Mn-Si alloys, this finding indicates that finely and homogeneously distributed M2 precipitates stabilize the CL, while coarse M2 particles have the opposite effect.

The lowest DR values were obtained for alloys of group III and for alloy I. In these alloys, the intermetallic phases are present in lower amounts and the precipitates are finely distributed (Figure 9). The absence of M121 and M2 coarse particles together with the homogeneous distribution of the fine compounds seems to contribute to reduce the DR of Mg-Si-Sr alloys.

When comparing the DR values with the increasing grain size values (see Figure 13b) no trend is observed. Then it can be stated that the influence of intermetallic phases as well as their size and distribution have a bigger influence on the DR than grain size for as-cast condition samples in this ternary system.

Conclusions

The microstructure and degradation performance of the Mg-Si-Sr system have been investigated and correlated. Scheil solidifications helped to interpret the observed microstructures. PDP and ML immersion tests were used to evaluate the alloy's corrosion behavior.

Similar trends have been observed when comparing the two different degradation tests. A strong dependence of the degradation performance on alloy composition, phase morphology and phase distribution has been deduced from the experiments. It has been also observed that the early reactions are more severe while degradation stabilizes with time.

The DR becomes too high when a high content of the $Mg_{17}Sr_2$ phase forms or by the presence of coarse particles of the intermetallics Mg_2Si, MgSiSr or $MgSi_2Sr$. When these phases form in a fine morphology the increase of DR is less significant. In cases where the amount of alloying elements, impurities or phase content was above a certain limit (concentration of alloying elements higher than 8wt.%, impurity level higher than 185 ppm or intermetallics presence above 14wt.%), the DR steeply increased.

On the other hand the DR was reduced compared to that of pure Mg for some alloy compositions. This is the case for alloys H and I with a total amount of alloying elements below 0.4wt% (keeping Sr below 0.25wt%) and impurity levels below 100 ppm. These alloy composition could be suitable for clinical use. It is therefore interesting to further investigate them in order to have longer period *in vitro* results and their *in vivo* behavior.

Acknowledgements

The authors want to specially acknowledge the help during the production process to Gabor Szakacs and in the mass loss measurements to Monika Luczak. Equally they want to mention the help and contribution in this work specially to Nachicketa Ray and Gokula Krishna Muralidharan. The research was supported by the PEOPLE programme (Marie Sklodowska-Curie Action) of the EU FP7 Programme FP7/ 2007-2013/ under REA grant agreement n°289163.

References

1. Witte, F., *The history of biodegradable magnesium implants: a review.* Acta biomaterialia, 2010. **6**(5): p. 1680-1692.
2. Zheng, Y.F., X.N. Gu, and F. Witte, *Biodegradable metals.* Materials Science and Engineering: R: Reports, 2014. **77**: p. 1-34.
3. Tie, D., et al., *Antibacterial biodegradable Mg-Ag alloys.* European cells & materials, 2012. **25**: p. 284-98; discussion 298.
4. Vlček, M., Lukač, F., Stulikova, I., Smola, B., Kudrnova, H., Vlach, M., Kodetova, V., Szakacs, G., Hort, N., Kainer, K.U. *Precipitation Processes in Mg-Y-Nd-Ag Alloys Suitable for Biodegradable Implants*. in *Metal 2014*. 2014. Brno, Czchec Republic.
5. Marco, I., Van der Biest, O., Feyerabend, F., Willumeit-Römer, R., *Comparison of the degradation behaviour of binary Mg-Ag and Mg-Gd alloys in PBS and in physiological conditions.* . European Cells and Materials 2014. **28 (3)** p. 42.
6. Zhang, E., et al., *Microstructure, mechanical properties and bio-corrosion properties of Mg–Si(–Ca, Zn) alloy for biomedical application.* Acta biomaterialia, 2010. **6**(5): p. 1756-1762.
7. Tie, D., et al., *An in vivo study on the metabolism and osteogenic activity of bioabsorbable Mg–1Sr alloy.* Acta biomaterialia, 2016. **29**: p. 455-467.
8. Suganthi, R.V., et al., *Fibrous growth of strontium substituted hydroxyapatite and its drug release.* Materials Science and Engineering: C, 2011. **31**(3): p. 593-599.
9. P.A. Revell, E.D., X.S. Zhang, P. Evans, C.R. Howlett, *The Effect of Magnesium Ions on Bone Bonding to Hydroxyapatite Coating on Titanium Alloy Implants.* Key Eng. Mater. , 2004. **254**(2): p. 447-450.
10. Zreiqat, H., et al., *Mechanisms of magnesium-stimulated adhesion of osteoblastic cells to commonly used orthopaedic implants.* Journal of Biomedical Materials Research, 2002. **62**(2): p. 175-184.
11. Bornapour, M., et al., *Biocompatibility and biodegradability of Mg–Sr alloys: The formation of Sr-substituted hydroxyapatite.* Acta biomaterialia, 2013. **9**(2): p. 5319-5330.
12. Dahl, S.G., et al., *Incorporation and distribution of strontium in bone.* Bone, 2001. **28**(4): p. 446-453.
13. Wu, K., et al., *A CALPHAD study on the thermodynamic stability of calcium-, zinc-, and yttrium-doped magnesium in aqueous environments.* Materials Science and Engineering: B, 2011. **176**(20): p. 1727-1732.
14. Thomas, S., et al., *Corrosion mechanism and hydrogen evolution on Mg.* Current Opinion in Solid State and Materials Science, 2015. **19**(2): p. 85-94.
15. Song, G., A. Atrens, and D. StJohn, *An Hydrogen Evolution Method for the Estimation of the Corrosion Rate of Magnesium Alloys*, in *Magnesium Technology 2001*2001, John Wiley & Sons, Inc. p. 254-262.
16. Kirkland, N., N. Birbilis, and M. Staiger, *Assessing the corrosion of biodegradable magnesium implants: a critical review of current methodologies and their limitations.* Acta biomaterialia, 2012. **8**(3): p. 925-936.

17. Marco, I., et al., *Degradation testing of Mg alloys in Dulbecco's modified eagle medium: Influence of medium sterilization.* Materials Science and Engineering: C, 2016. **62**: p. 68-78.
18. Ghali, E., *2 - Activity and passivity of magnesium (Mg) and its alloys*, in *Corrosion of Magnesium Alloys*, G.-l. Song, Editor 2011, Woodhead Publishing. p. 66-114.
19. Marco, I. and O. Van der Biest, *Polarization measurements from a rotating disc electrode for characterization of magnesium corrosion.* Corrosion Science, 2016. **102**: p. 384-393.
20. Bender, S., et al., *Corrosion and corrosion testing of magnesium alloys.* Materials and Corrosion, 2007. **58**(12): p. 977-982.
21. *Standard practice for laboratory immersion corrosion testing of metals.*, in *ASTM G31-72*2004: Annual book of ASTM standards. Philadelphia; PA:ASTM.
22. Chou, D.-T., et al., *In vitro and in vivo corrosion, cytocompatibility and mechanical properties of biodegradable Mg–Y–Ca–Zr alloys as implant materials.* Acta biomaterialia, 2013. **9**(10): p. 8518-8533.
23. Lisitsyn, V., et al., *The role of Ca microalloying on the microstructure and corrosion behavior of Mg–6Zn–Mn–(0.5–2)Si alloys.* Corrosion Science, 2009. **51**(4): p. 776-784.
24. Hofstetter, J., et al., *Assessing the degradation performance of ultrahigh-purity magnesium in vitro and in vivo.* Corrosion Science, 2015. **91**: p. 29-36.
25. Song, G.L. and A. Atrens, *Corrosion Mechanisms of Magnesium Alloys.* Advanced Engineering Materials, 1999. **1**(1): p. 11-33.
26. Hillis, J.E. and K. Reichek, *High Purity Magnesium AM60 Alloy: The Critical Contaminant Limits and the Salt Water Corrosion Performance.* SAE transactions, 1986(2): p. 227-234.
27. J. Hanawalt, C.N., J. Peloubet, *Corrosion studies of magnesium and its alloys.* American Institute of Mining and Metallurgical Engineers (AIME), 1942. **147**: p. 273-299.
28. H. E. Friedrich, B.L.M., *Metallurgy, Design Data, Applications*, in *Magnesium Technology*2006, Springer-Verlag Berlin Heidelberg. p. 122-124.
29. Gu, X., et al., *In vitro corrosion and biocompatibility of binary magnesium alloys.* Biomaterials, 2009. **30**(4): p. 484-498.
30. Zeng, R., et al., *Progress and Challenge for Magnesium Alloys as Biomaterials.* Advanced Engineering Materials, 2008. **10**(8): p. B3-B14.
31. Krause, A., et al., *Degradation behaviour and mechanical properties of magnesium implants in rabbit tibiae.* Journal of Materials Science, 2010. **45**(3): p. 624-632.
32. Gu, X.N., et al., *In vitro and in vivo studies on a Mg–Sr binary alloy system developed as a new kind of biodegradable metal.* Acta biomaterialia, 2012. **8**(6): p. 2360-2374.
33. Zeng, X., et al., *Effect of strontium on the microstructure, mechanical properties, and fracture behavior of AZ31 magnesium alloy.* Metallurgical and Materials Transactions A, 2006. **37**(4): p. 1333-1341.
34. Bornapour, M., et al., *Magnesium implant alloy with low levels of strontium and calcium: The third element effect and phase selection improve bio-corrosion resistance and mechanical performance.* Materials Science and Engineering: C, 2014. **35**: p. 267-282.
35. Brar, H.S., J. Wong, and M.V. Manuel, *Investigation of the mechanical and degradation properties of Mg–Sr and Mg–Zn–Sr alloys for use as potential biodegradable implant materials.* Journal of the Mechanical Behavior of Biomedical Materials, 2012. **7**: p. 87-95.
36. Li, Y., et al., *Mg–Zr–Sr alloys as biodegradable implant materials.* Acta biomaterialia, 2012. **8**(8): p. 3177-3188.
37. Ben-Hamu, G., D. Eliezer, and K.S. Shin, *The role of Mg2Si on the corrosion behavior of wrought Mg–Zn–Mn alloy.* Intermetallics, 2008. **16**(7): p. 860-867.
38. Srinivasan, A., et al., *Influence of Si and Sb additions on the corrosion behavior of AZ91 magnesium alloy.* Intermetallics, 2007. **15**(12): p. 1511-1517.
39. Mingbo, Y. and S. Jia, *Modification and refinement mechanism of Mg2Si phase in Sr-containing AZ61-0.7 Si magnesium alloy.* Research & Development, 2009.
40. Gil-Santos, A., et al., *Identification and description of intermetallic compounds in Mg–Si–Sr cast and heat-treated alloys.* Journal of Alloys and Compounds, 2016. **669**: p. 123-133.

41. Scheil, E., *Bemerkungen zur schichtkristallbildung.* Z. Metallk, 1942. **37**: p. 70-72.
42. Gulliver, G., *The quantitative effect of rapid cooling upon the constitution of binary alloys.* The Journal of the Institute of Metals, 1913. **9**: p. 120.
43. Schmid-Fetzer, R., *Phase Diagrams: The Beginning of Wisdom.* Journal of Phase Equilibria and Diffusion, 2014. **35**(6): p. 735-760.
44. Schmid-Fetzer, R., *Personal communication MgSiSr_v7 database*, 2016.
45. Schille, C., et al., *Corrosion of experimental magnesium alloys in blood and PBS: A gravimetric and microscopic evaluation.* Materials Science and Engineering: B, 2011. **176**(20): p. 1797-1801.
46. Xin, Y., T. Hu, and P.K. Chu, *Influence of test solutions on in vitro studies of biomedical magnesium alloys.* Journal of The Electrochemical Society, 2010. **157**(7): p. C238-C243.
47. McCafferty, E., *Validation of corrosion rates measured by the Tafel extrapolation method.* Corrosion Science, 2005. **47**(12): p. 3202-3215.
48. Cipriano, A., et al., *In vitro degradation of four magnesium–zinc–strontium alloys and their cytocompatibility with human embryonic stem cells.* Journal of Materials Science: Materials in Medicine, 2013. **24**(4): p. 989-1003.
49. Guan, R.-G., et al., *Development and evaluation of a magnesium-zinc-strontium alloy for biomedical applications - Alloy processing, microstructure, mechanical properties, and biodegradation.* Materials Science and Engineering: C, 2013. **33**(7): p. 3661-3669.